ARTICLE

doi:10.1038/nature09818

Wiring specificity in the direction-selectivity circuit of the retina

Kevin L. Briggman[1], Moritz Helmstaedter[1] & Winfried Denk[1]

The proper connectivity between neurons is essential for the implementation of the algorithms used in neural computations, such as the detection of directed motion by the retina. The analysis of neuronal connectivity is possible with electron microscopy, but technological limitations have impeded the acquisition of high-resolution data on a large enough scale. Here we show, using serial block-face electron microscopy and two-photon calcium imaging, that the dendrites of mouse starburst amacrine cells make highly specific synapses with direction-selective ganglion cells depending on the ganglion cell's preferred direction. Our findings indicate that a structural (wiring) asymmetry contributes to the computation of direction selectivity. The nature of this asymmetry supports some models of direction selectivity and rules out others. It also puts constraints on the developmental mechanisms behind the formation of synaptic connections. Our study demonstrates how otherwise intractable neurobiological questions can be addressed by combining functional imaging with the analysis of neuronal connectivity using large-scale electron microscopy.

The computation of motion direction by direction-selective retinal ganglion cells (DSGCs), discovered almost 50 years ago[1], has defied comprehensive explanation, partly because the wiring diagram of the neuronal circuit underlying this computation is still not known in sufficient detail. DSGCs respond strongly to motion oriented along a preferred direction, but not to null-direction (where null direction is 180° from the preferred direction) motion. In theory, this asymmetry could arise from increased inhibition during null-direction motion, increased excitation during preferred-direction motion, or through a combination of both mechanisms. The asymmetry could be implemented at the structural level, in the wiring of the direction-selectivity circuitry, or could result from unequal synaptic strengths in an otherwise structurally symmetric circuit. Barlow and Levick[2] favoured a mechanism involving the selective pre-emption of responses during null-direction motion by lateral inhibition. The magnitude of the inhibitory synaptic input to DSGCs is indeed spatially asymmetric, as patch-clamp recordings from DSGCs have shown[3,4]. The main source of this inhibition is starburst amacrine cells (SACs), retinal interneurons[5,6] that are necessary in the direction-selectivity circuit[7] and release both GABA (γ-aminobutyric acid) and acetylcholine[8]. Furthermore, SAC dendrites have been shown to be direction-selective, preferring centrifugal motion[9].

Asymmetric connectivity between SACs and DSGCs forms the basis of most models for how direction selectivity is computed[4,10–15]. Dual whole-cell recordings have shown inhibitory connections between SACs and DSGCs to be stronger when the SAC's soma is located on the null side (that is, the side from which null-direction stimuli approach) of the DSGC's soma[4,16,17]. However, it is not known whether individual synapses from null-side SACs have a higher unitary conductance[16–18], for example, as a result of developmental strengthening[19], or, alternatively, whether this functional asymmetry is due to an increased number of synaptic contacts. It is also unknown whether synapse formation or strengthening is dependent mainly on the relative location of SAC and DSGC somata or rather on the direction of the SAC dendritic branch. The latter would be expected if each DSGC optimally collects appropriately selective input signals from SAC dendrites. Both questions are difficult to address solely by physiological means. Rather, structural information about the location of individual SAC-to-DSGC synaptic contacts and the direction of the pre-synaptic SAC dendrites is needed.

Attempts to study direction-selectivity circuit anatomy by light microscopy have led to contradictory results, with some reports[4] showing a higher number of neurite proximities from null-side SACs and others not[20–22]. Electron microscopy studies of the direction-selectivity circuit[5,23] have, on the other hand, not been able to reconstruct large fractions of SACs and DSGCs in the same piece of tissue. This illustrates the general difficulty of acquiring and analysing three-dimensional ultrastructural data to determine neural circuit diagrams. Such data need to have sufficient resolution to reliably follow small calibre (as small as a few tens of nanometres) neuronal processes and, at the same time, need to cover the spatial distances over which individual neurons project, typically at least some hundreds of micrometres.

Serial-section electron microscopy (SSEM), which was used for the reconstruction of the *Caenorhabditis elegans* nervous system[24], is laborious, uses thicker sections and data are occasionally corrupted by sectioning and imaging artefacts. These problems are ameliorated by automating the acquisition of EM data, as in serial block-face electron microscopy (SBEM)[25]. SBEM provides the necessary three-dimensional resolution and field of view to follow thin neurites across hundreds of micrometres of complex neuropil.

What complicates the purely anatomical analysis of the direction-selectivity circuit is that a DSGC's preferred direction cannot be deduced from its dendritic morphology[26,27]. We, therefore, combined two-photon functional calcium imaging in the intact retina[28] with a SBEM-based reconstruction of the SAC–DSGC circuitry in the same piece of tissue. We found a strong asymmetry in the number of synaptic contacts, most of which are from SAC dendrites that are roughly oriented along the null direction of DSGCs, supporting a mechanism of null-direction inhibition. We also found evidence that the orientation of an individual SAC dendrite rather than the axis between the SAC and DSGC somata determines whether or not a synapse forms.

[1]Max Planck Institute for Medical Research, Department of Biomedical Optics, Heidelberg 69120, Germany.

Functional and structural identification of DSGCs

To identify the preferred directions of On–Off DSGCs, we labelled the ganglion cell layer of an adult mouse retina by bulk electroporation[48] with the membrane-impermeable form of Oregon Green 488 BAPTA-1, a calcium indicator. This avoids the damage that would inevitably result from the pipette penetration needed for acetoxymethyl ester-based loading[29,30] and would possibly result from exposing the retina to the detergents used during this procedure. We then used two-photon-excited fluorescence imaging[31] to characterize the response properties of ganglion cells while projecting moving-bar stimuli (oriented in eight equally spaced directions) onto the photoreceptors[32]. We imaged 634 neuronal somata in a 300 µm by 300 µm large region of the ganglion cell layer (Fig. 1b). Among those were 25 On–Off DSGCs with preferred directions clustering in 4 groups (Fig. 1a and Supplementary Fig. 1). We denoted those groups, which are known to correspond to the cardinal visual axes[33], as northward (N), eastward (E), southward (S) and westward (W). The cells (6 N, 8 E, 7 S, and 4 W) were arranged in a mosaic pattern (Fig. 1b). Immediately after two-photon imaging, we fixed and stained the retina (see Methods) and prepared it for SBEM. To assist traceability, the tissue was specially treated to preferentially label cell surfaces and to leave intracellular structures unstained. The acquired SBEM volume was $350 \times 300 \times 60\ \mu m^3$ in extent, spanned the inner plexiform layer, and contained the ganglion cell layer and part of the inner nuclear layer. The lateral resolution was 16.5 nm × 16.5 nm and the section thickness (z-resolution) was 23 nm. All calcium-imaged somata (Fig. 1c) were included in the acquired SBEM volume.

Vasculature landmarks were used to identify the somata of the recorded DSGCs in the SBEM volume (Fig. 1c). Beginning at their somata, we traced the dendritic trees of six DSGCs (Fig. 2a; 2 N, 1 E, 1 S and 2 W cells). Instead of contouring each dendrite, we traced skeletons along the centre lines of the dendrites, which speeds up the tracing process considerably (M. Helmstaedter, K. L. Briggman and W. Denk, manuscript submitted). The resulting dendritic trees all ramified in two distinct sublayers in the inner plexiform layer and overlapped each other horizontally (Fig. 2a, b). The output synapses of SACs are formed at varicosities along the distal third of their dendrites[5] and are geometrically conspicuous, with the presynaptic varicosity wrapping around postsynaptic dendrites[34]. We, therefore, identified such varicose contacts (Fig. 3a, $n = 24$ contacts) on both the On and Off dendrites of each of the DSGCs and traced the putative presynaptic neurites back to their respective somata. Starting at these somata, we then skeletonized most of their dendritic trees, which substantially overlapped the dendritic fields of the DSGCs (Fig. 2c and Supplementary Figs 2 and 7). In every instance, the back-traced cell was a SAC, recognizable by its radially symmetric morphology and co-stratification with either On or Off DSGC arborizations ($n = 11$ On, 13 Off SACs). Given an estimated SAC density (including On and Off SACs) of 2,000 mm^{-2} for the mouse[35], we skeletonized 11% of all SAC somata in the data set.

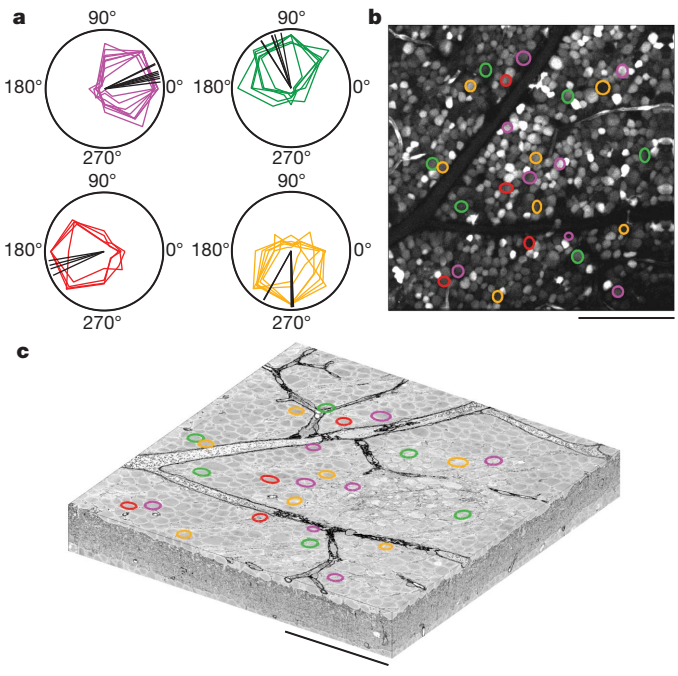

Figure 1 | Functional characterization of DSGCs and their localization within the SBEM volume. **a**, Polar tuning curves for 25 DSGCs sorted and colour-coded by preferred direction. Black lines indicate the direction of the vector-summed responses. **b**, **c**, The corresponding soma locations superimposed onto a two-photon image from the recorded region of the ganglion cell layer (**b**) and the acquired SBEM volume (**c**). Note the Y-shaped blood vessel visible in both **b** and **c**. Scale bars are 100 µm.

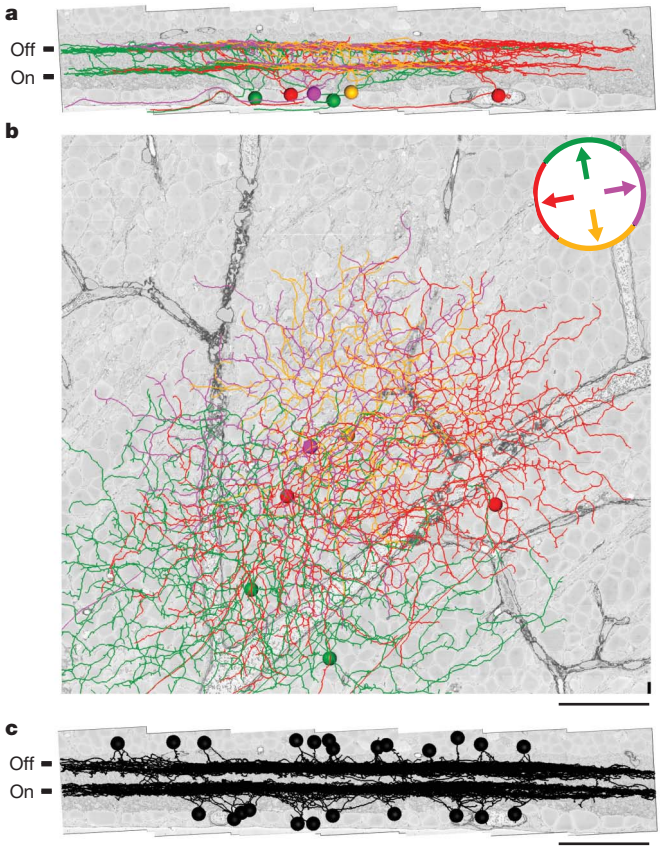

Figure 2 | Skeleton reconstructions of DSGCs and SACs. **a**, **b**, DSGCs, colour-coded by preferred direction (inset), projected parallel to (**a**) and normal to (**b**) the plane of the retina. Note bi-stratification in the inner plexiform layer. **c**, Parallel projections of 24 SACs (11 On SACs, 13 Off SACs, black). Scale bars are 50 µm.

Synaptic connections between SACs and DSGCs

To identify all additional potential contacts between the 24 SACs and 6 DSGCs that were reconstructed, we next inspected all locations where a SAC and a DSGC skeleton came within 1.5 µm of each other. Of 9,260 such locations, 831 were varicose contacts and were marked as putative synapses (Fig. 3a). In 2,650 other cases, a non-varicose, thin part of a SAC dendrite touched a DSGC dendrite (Fig. 3c). Such configurations were marked as 'incidental' contacts and are expected owing to the tight co-fasciculation of SAC and DSGC dendrites[5]. We occasionally found a configuration (Fig. 3e) where a SAC varicosity and a DSGC dendrite came within tens of nanometres of each other

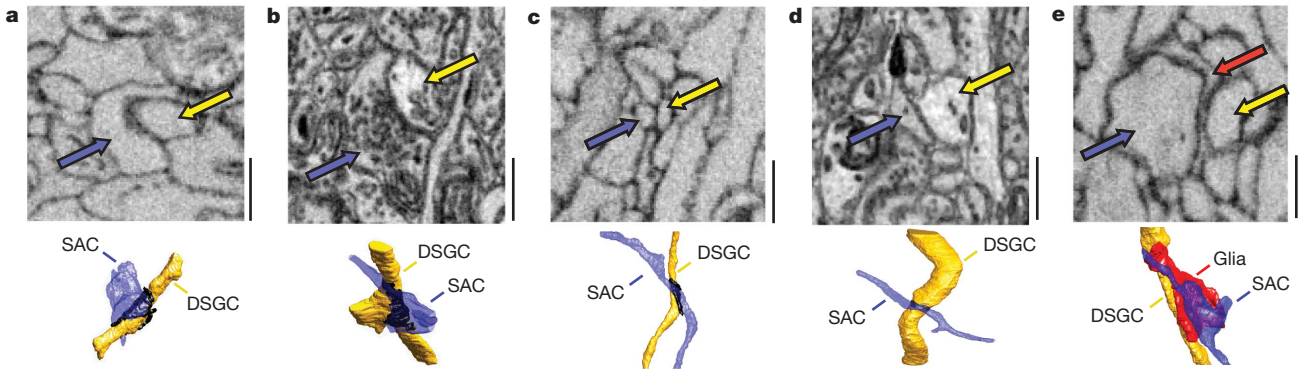

Figure 3 | Contact geometries. **a**, Typical putative synaptic contact in the surface-labelled sample in cross-section and as a three-dimensional rendering, with the contact area in black. **b**, Identified SAC-to-DSGC synapse in the conventionally stained SBEM volume. Note vesicles associated with the presynaptic surface and the dense staining of the contact. In both **a** and **b**, the SAC varicosity (blue) wraps around the DSGC dendrite (yellow). **c**, **d**, Incidental contacts (thin regions of SAC and DSGC dendrites touching) in the surface-labelled (**c**) and the conventionally stained SBEM (**d**) volumes. **e**, SAC varicosity located very close to a DSGC, but separated by a thin Müller-cell glial process (red). Scale bars are 500 nm.

but did not make any direct contact and were instead separated by a thin, sheet-like process (probably from a Müller glia cell). Such appositions would probably be misconstrued as actual contacts using even the highest possible resolution in the (diffraction-limited) light microscope.

To confirm that the putative synapses are likely to be actual synapses, we examined varicose SAC–DSGC contacts in a different SBEM data set that was more conventionally stained (Fig. 3b). All varicose contacts inspected in this data set ($n = 43$) contained ultrastructural details typical of synapses. In addition, no synaptic specializations were seen at incidental SAC–DSGC contacts in this data set (Fig. 3d). The following analysis includes only the 831 contacts that were marked as putative synapses in the surface-stained data set (henceforth referred to as 'synapses').

We first examined the specificity of SAC–DSGC synapses from the perspective of individual SACs. We chose one Off and one On SAC (Fig. 4a and Supplementary Fig. 3) that each overlapped with the six DSGCs and colour-coded their output synapses by the preferred directions of the respective DSGCs (Fig. 4b; purple, E; green, N; red, W; orange, S). In addition, we identified all of the remaining varicosities on the dendrites of these two SACs (413 On SAC; 452 Off SAC; black dots in Fig. 4a and Supplementary Fig. 3). Output synapses preferred DSGCs with a preferred direction antiparallel to the SAC dendrite (and hence aligned with the null direction). For example, the northward oriented branches of the SACs mostly synapsed onto the southward preferring (orange) DSGC. Despite a large overlap of these northward branches with the dendritic trees of a westward (red) and eastward (purple) DSGC (Fig. 4a), they avoided synapsing onto them. The specificity is even more apparent in the outputs to the two westward (red) DSGCs. This pattern of specificity was found across all reconstructed SACs (Fig. 4b). A given SAC branch does not exclusively synapse onto only one type of DSGC; synapses onto DSGCs with different preferred directions sometimes occur, in particular for dendrites oriented in between the cardinal directions. We observed no obvious difference in the selectivity between On and Off sublayers (data not shown).

We next examined the specificity of synapses from the perspective of individual DSGCs. For each SAC–DSGC synapse, we constructed a vector oriented from its presynaptic SAC soma to the synapse location (Fig. 5a and Supplementary Fig. 5). We measured the angle (dendrite angle) between this vector and the 0° stimulus direction. The distribution of dendrite angles was strongly non-uniform for each DSGC (Fig. 5b), with most SAC dendrites oriented opposite to the DSGC's preferred direction (Fig. 5c). The difference between dendrite angle and preferred direction was 165.2° ± 51.7° (mean ± s.d., $n = 831$). A similar distribution of dendrite angles was observed in the conventionally stained retina data set (Supplementary Fig. 4), where, however, the preferred direction of the DSGC was not a priori known. Consistent with electrophysiological recordings, which found a higher

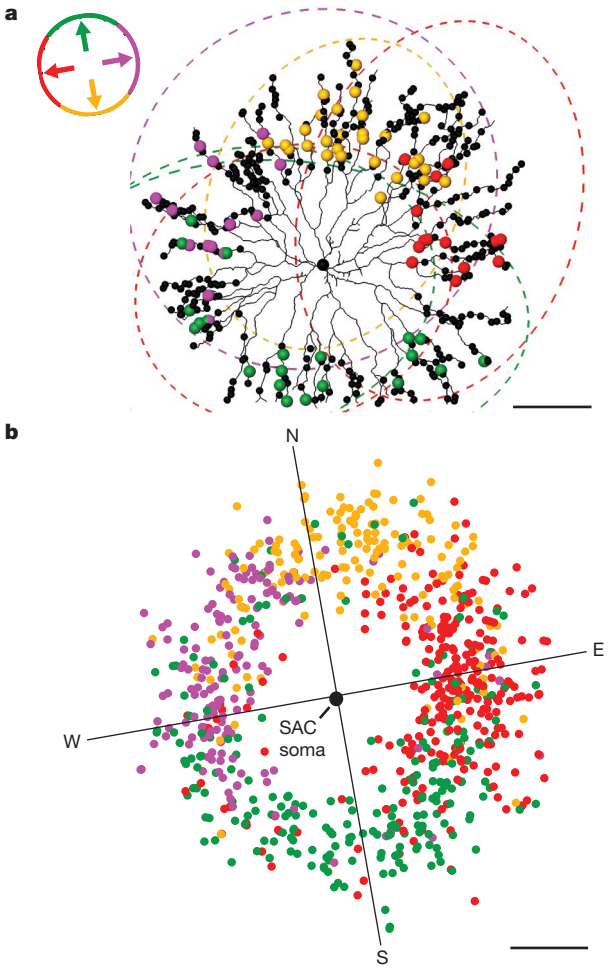

Figure 4 | Specificity of SAC outputs. **a**, An Off SAC (black skeleton), with varicosities indicated by black dots. DSGC dendritic trees are indicated by colour-coded dashed ellipses. Synapses are colour-coded by the preferred direction of the postsynaptic DSGC. **b**, Output synapse locations ($n = 831$ synapses) relative to SAC somata from all 24 SACs. Scale bars are 50 µm.

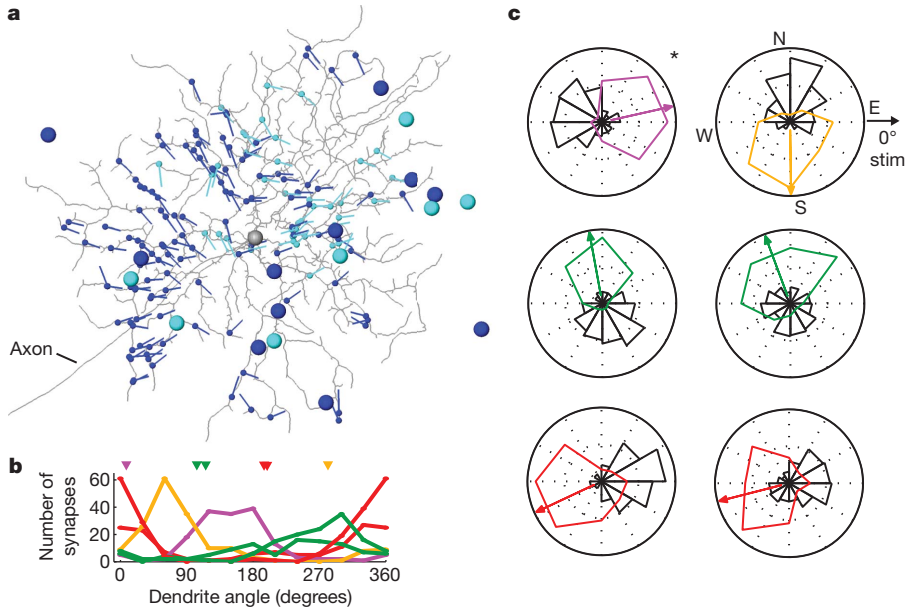

Figure 5 | Specificity of DSGC inputs. **a**, DSGC (grey skeleton) and the connected On and Off SAC somata (large cyan and blue circles, respectively) and associated SAC input synapses (smaller cyan and blue circles) from 18 SACs. **b**, The distribution of all SAC dendrite angles (θ_{dendr}) for each of the six DSGCs; θ_{dendr} is defined by the vectors (cyan and blue lines in **a**) oriented from SAC somata to synapse location. Triangle markers indicate the preferred direction for each DSGC. **c**, Polar histograms of θ_{dendr} (black, plotted as the square root of θ_{dendr} frequencies) together with the DSGC tuning curves (as in Fig. 1). Asterisk denotes the DSGC shown in **a**.

overall inhibitory conductance driven by SACs located on the null side[4,16–18], we found a larger number of synapses received from null-side versus preferred-side SAC somata (524 versus 41 synapses, where ND indicates null direction; $|\theta_{soma} - \theta_{ND}| < 45^\circ$ versus $|\theta_{soma} - \theta_{ND}| > 135^\circ$; Fig. 6b).

Although we found a strong correlation between SAC dendrite angles and DSGC null directions, we have not ruled out that the probability of forming a synapse between a SAC and a DSGC dendrite is solely determined by the relative locations of the corresponding somata, that is, by the angle between the null direction and the SAC-soma–DSGC-soma axis (Fig. 6a). In this case the connectivity should not depend on whether a dendrite is aligned more or less closely with the null direction than the soma–soma axis (Fig. 6a, upper panel); however, if, instead, the dendrite angle is the determinant then it should (Fig. 6a, lower panel). Our analysis (Fig. 6b) shows that for dendrite angles closer to the null direction ($\gamma < 0^\circ$) the actual connectivity is substantially higher. This is not caused by uneven sampling because the distribution of all contacts (incidental and varicose, Fig. 6c) is unbiased. We found the strongest bias when the soma–soma axis is between 45° and 135° off the null direction (Fig. 6b; $\gamma < 0^\circ$ for 75.2% of the synapses). We also calculated the mean of γ separately for different soma–soma angle ranges (Fig. 6d). In the range from 45° to 135°, the connected dendrites run 24.3° ± 2.8° (mean ± s.e.m.) closer to the null direction.

Discussion

Our data show that SAC dendrites selectively synapse with a DSGC if they are oriented along its null direction. This pattern provides the structural substrate for the functional asymmetry in the inhibitory input currents observed in DSGCs[3,4]. The wiring specificity is apparent both from the perspective of the SACs' outputs (Fig. 4) and that of the DSGCs' inputs (Fig. 5). Dendritic branches of SACs are individually direction selective for centrifugal motion[9], with several mechanisms likely to contribute[36–38]. Our data support the view that DSGCs acquire their direction selectivity by predominately collecting those SAC inputs that suppress null-direction excitation, that is, from branches oriented along the null direction, and are consistent with the idea that null-direction SAC input inhibits the initiation of DSGC dendritic spikes during null-direction motion[14].

The specificity of each SAC dendritic branch for selecting a postsynaptic target goes well beyond the notion that neuron A selectively

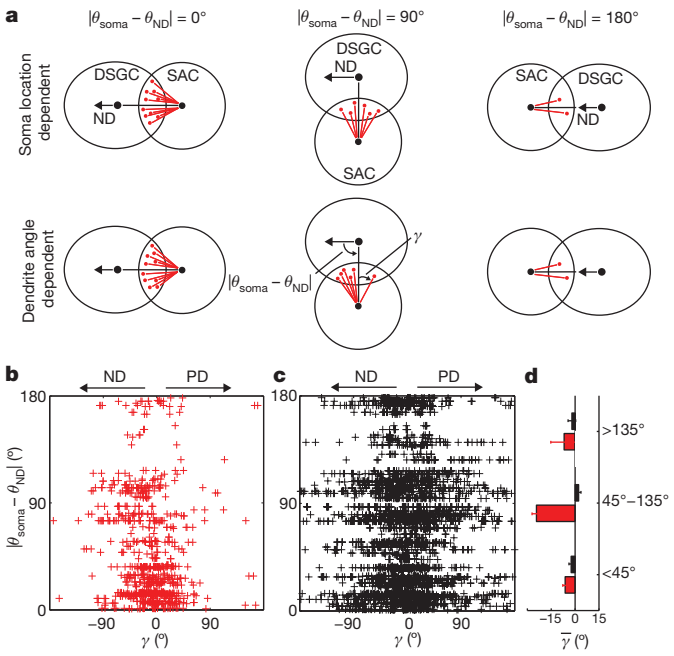

Figure 6 | Dendrite-angle distribution. **a**, Schematic synapse distributions expected for a mechanism depending only on soma angles (upper) and for a mechanism instead depending on dendrite angles (lower). The soma angle $|\theta_{soma} - \theta_{ND}|$ and relative dendrite angle $\gamma = (\theta_{soma} - \theta_{dendr}) \times \text{sign}(\theta_{soma} - \theta_{ND})$ are indicated, with $\gamma < 0$ indicating dendrite directions closer to the null direction than the soma–soma vector. **b**, Angular distribution of synapses ($n = 831$). **c**, Distribution of all synapses and incidental touches ($n = 3{,}481$). **d**, The mean ± s.e.m. for γ in three different ($\theta_{soma} - \theta_{ND}$) ranges.

wires to neuron B, which is all that electrophysiological measurements can test. Instead the dendrite angle has an additional, perhaps dominant, role (Fig. 6), which is consistent with SAC dendrites acting as independent computational units[9]. This implies that the mechanism that determines whether an actual synapse is formed cannot depend on cell identities alone but uses the local dendrite geometry or activity.

SAC synapses onto DSGCs (Fig. 5) are not restricted to the null-side half of the DSGC dendritic tree but can be found across the entire dendritic field (Fig. 5a and Supplementary Fig. 5). Because SACs and DSGCs have similar dendritic-field diameters, some somata of strongly connected SACs lie near or actually on the preferred side of a DSGC's soma (Fig. 5a and Supplementary Fig. 5). This arrangement is consistent with the observation that DSGCs are direction-selective for local motion (that is, motion of a small spot within the dendritic field)[2], and also supports the notion that asymmetric null-direction lateral inhibition underlies the non-discriminating zone along the preferred-side edge of DSGC receptive fields[2,39].

We have presumed that the asymmetrically arranged SAC synapses are GABAergic, consistent with paired SAC–DSGC recordings[4,16,17] and the finding that GABA antagonists block direction-selective responses in DSGCs[40,41]. SACs also synthesize and release acetylcholine[6,8,42], but the role of acetylcholine in the direction-selectivity circuit remains unclear[13]. Some models[11,15] argue that, in addition to asymmetric GABA release during null-direction motion, acetylcholine excites DSGCs asymmetrically during preferred-direction motion, leading to a SAC-generated 'push–pull' mechanism. Such a mechanism would, however, require contacts from preferred-direction-oriented dendrites, which are very sparse (Fig. 5). Further analysis of our EM data sets should reveal whether a different type of push–pull mechanism is present, whereby bipolar-cell terminals are inhibited[23] in a direction-specific manner.

Cholinergic currents have been recorded in DSGCs during both preferred-direction and null-direction motion[43]. A study[17] of SAC–DSGC connectivity found direction-selective GABA but non-direction-selective acetylcholine currents, suggesting that the release of the two transmitters and/or their receptors are spatially segregated. The low number of preferred-direction-oriented synapses and a fraction of null-direction-oriented synapses could provide symmetric synaptic acetylcholine signalling. Alternatively, the effect of acetylcholine could be largely paracrine, which is supported by the extrasynaptic localization of nicotinic receptors[44] and the existence of both nicotinic and muscarinic acetylcholine receptors remote from the choline-acetyltransferase-positive layers and thus distant to SAC dendrites[34,45], the sole source of acetylcholine in the retina[6]. The tight co-fasciculation of DSGC and SAC dendrites means short distances and therefore fast diffusion, in agreement with the fast rise times and latencies observed for cholinergic connections[17].

The ultrastructure of synapses in the direction-selectivity circuit has been previously studied[5,23], but only the ability to collect a large enough EM volume at sufficient resolution made it possible to also study the directionality of presynaptic SAC dendrites. Combining, in the same piece of tissue, prior functional imaging and SBEM imaging allowed us to both target DSGCs for reconstruction and make a direct correlation between circuit structure and function. To trace the thin dendrites of SACs across hundreds of micrometres, the high z-resolution (23-nm section thickness) proved crucial. Furthermore, the prevalence of close encounters between neurites makes it unlikely (Fig. 3c–e) that a reliable determination of connectivity in the direction-selectivity circuit could ever be performed by fluorescent co-localization, but instead requires EM resolution.

The approach used here—tracing a cell and then going on to trace synaptically connected cells—is a virtual version of trans-synaptic-virus tracing[46,47]. Although not (yet) providing the spatial reach of real virus methods, our approach, unlike those, does reveal the strength of connections in terms of the number of contacts, with an analysis of contact areas possible when needed. Whereas the current study relied on targeted sparse reconstructions, similar SBEM data can, and probably will, be used for the dense (connectomic) reconstruction of the complete retinal circuitry.

METHODS SUMMARY

Calcium imaging. A dark-adapted retina from a wild-type C57BL/6 mouse was filled with the calcium indicator Oregon Green 488 BAPTA-1 by parallel-plate electroporation and imaged in a custom-built two-photon microscope during through-the-objective stimulation with bright bars moving in eight different directions at 0.5 mm s^{-1}. Sulphorhodamine 101 fluorescence was used to visualize the vasculature. Calcium imaging data were analysed using custom Matlab routines.

Tissue preparation for SBEM. The retina was incubated in 5 mg ml^{-1} horseradish peroxidase before fixation in 0.1 M cacodylate buffer with 4% sucrose and 2% glutaraldehyde, DAB precipitation in phosphate buffer with 4% sucrose, 5.6 mM DAB and 1.4 mM H_2O_2, staining in 2% aqueous osmium tetroxide, enhancing by en bloc lead citrate, ethanol-series dehydration, and embedding in Epon hard. A second, not calcium-imaged, retina was more conventionally stained.

SBEM imaging and data analysis. The two-photon imaged region was mounted in a custom-built ultra-microtome operating inside the chamber of a field-emission scanning electron microscope (FEI QuantaFEG 200) and serial block-face imaged in 50 Pa water vapour at 2.5 keV landing energy at a dose of 10 electrons per nm^2 and a resolution of $16.5 \times 16.5 \times 23$ nm^3 (for the conventionally stained sample, see Methods). A custom-designed back-scattered electron detector was used. SBEM data were aligned and stitched using custom Matlab routines. Skeletons were manually traced using custom written (KNOSSOS) software. Volumes were traced using ITK-SNAP.

Full Methods and any associated references are available in the online version of the paper at www.nature.com/nature.

Received 20 October 2010; accepted 10 January 2011.

1. Barlow, H. B., Hill, R. M. & Levick, W. R. Retinal ganglion cells responding selectively to direction and speed of image motion in the rabbit. *J. Physiol. (Lond.)* **173,** 377–407 (1964).
2. Barlow, H. B. & Levick, W. R. The mechanism of directionally selective units in rabbit's retina. *J. Physiol. (Lond.)* **178,** 477–504 (1965).
3. Taylor, W. R. & Vaney, D. I. Diverse synaptic mechanisms generate direction selectivity in the rabbit retina. *J. Neurosci.* **22,** 7712–7720 (2002).
4. Fried, S. I., Munch, T. A. & Werblin, F. S. Mechanisms and circuitry underlying directional selectivity in the retina. *Nature* **420,** 411–414 (2002).
5. Famiglietti, E. V. Synaptic organization of starburst amacrine cells in rabbit retina: analysis of serial thin sections by electron microscopy and graphic reconstruction. *J. Comp. Neurol.* **309,** 40–70 (1991).
6. Tauchi, M. & Masland, R. H. The shape and arrangement of the cholinergic neurons in the rabbit retina. *Proc. R. Soc. Lond. B* **223,** 101–119 (1984).
7. Yoshida, K. *et al.* A key role of starburst amacrine cells in originating retinal directional selectivity and optokinetic eye movement. *Neuron* **30,** 771–780 (2001).
8. O'Malley, D. M., Sandell, J. H. & Masland, R. H. Co-release of acetylcholine and GABA by the starburst amacrine cells. *J. Neurosci.* **12,** 1394–1408 (1992).
9. Euler, T., Detwiler, P. B. & Denk, W. Directionally selective calcium signals in dendrites of starburst amacrine cells. *Nature* **418,** 845–852 (2002).
10. Chiao, C. C. & Masland, R. H. Starburst cells nondirectionally facilitate the responses of direction-selective retinal ganglion cells. *J. Neurosci.* **22,** 10509–10513 (2002).
11. Grzywacz, N. M., Tootle, J. S. & Amthor, F. R. Is the input to a GABAergic or cholinergic synapse the sole asymmetry in rabbit's retinal directional selectivity? *Vis. Neurosci.* **14,** 39–54 (1997).
12. Taylor, W. R. & Vaney, D. I. New directions in retinal research. *Trends Neurosci.* **26,** 379–385 (2003).
13. Demb, J. B. Cellular mechanisms for direction selectivity in the retina. *Neuron* **55,** 179–186 (2007).
14. Schachter, M. J. *et al.* Dendritic spikes amplify the synaptic signal to enhance detection of motion in a simulation of the direction-selective ganglion cell. *PLOS Comput. Biol.* **6** (2010).
15. Borg-Graham, L. J. The computation of directional selectivity in the retina occurs presynaptic to the ganglion cell. *Nature Neurosci.* **4,** 176–183 (2001).
16. Wei, W., Hamby, A. M., Zhou, K. & Feller, M. B. Development of asymmetric inhibition underlying direction selectivity in the retina. *Nature* **469,** 402–406 (2010).
17. Lee, S., Kim, K. & Zhou, Z. J. Role of ACh-GABA co-transmission in detecting image motion and motion direction. *Neuron* **68,** 1159–1172 (2010).
18. Yonehara, K. *et al.* Spatially asymmetric reorganization of inhibition establishes a motion-sensitive circuit. *Nature* **469,** 407–410 (2010).
19. Mumm, J. S. *et al.* Laminar circuit formation in the vertebrate retina. *Prog. Brain Res.* **147,** 155–169 (2005).
20. Famiglietti, E. V. A structural basis for omnidirectional connections between starburst amacrine cells and directionally selective ganglion cells in rabbit retina, with associated bipolar cells. *Vis. Neurosci.* **19,** 145–162 (2002).

21. Dong, W. *et al.* Dendritic relationship between starburst amacrine cells and direction-selective ganglion cells in the rabbit retina. *J. Physiol. (Lond.)* **556,** 11–17 (2004).
22. Chen, Y. C. & Chiao, C. C. Symmetric synaptic patterns between starburst amacrine cells and direction selective ganglion cells in the rabbit retina. *J. Comp. Neurol.* **508,** 175–183 (2008).
23. Dacheux, R. F., Chimento, M. F. & Amthor, F. R. Synaptic input to the on-off directionally selective ganglion cell in the rabbit retina. *J. Comp. Neurol.* **456,** 267–278 (2003).
24. White, J. G. *et al.* The structure of the nervous system of the nematode Caenorhabditis elegans. *Phil. Trans. R. Soc. Lond.* **314,** 1–340 (1986).
25. Denk, W. & Horstmann, H. Serial block-face scanning electron microscopy to reconstruct three-dimensional tissue nanostructure. *PLoS Biol.* **2,** e329 (2004).
26. Oyster, C. W., Amthor, F. R. & Takahashi, E. S. Dendritic architecture of ON-OFF direction-selective ganglion cells in the rabbit retina. *Vision Res.* **33,** 579–608 (1993).
27. Yang, G. & Masland, R. H. Receptive fields and dendritic structure of directionally selective retinal ganglion cells. *J. Neurosci.* **14,** 5267–5280 (1994).
28. Denk, W. & Detwiler, P. B. Optical recording of light-evoked calcium signals in the functionally intact retina. *Proc. Natl Acad. Sci. USA* **96,** 7035–7040 (1999).
29. Blankenship, A. G. *et al.* Synaptic and extrasynaptic factors governing glutamatergic retinal waves. *Neuron* **62,** 230–241 (2009).
30. Stosiek, C. *et al. In vivo* two-photon calcium imaging of neuronal networks. *Proc. Natl Acad. Sci. USA* **100,** 7319–7324 (2003).
31. Denk, W., Strickler, J. H. & Webb, W. W. Two-photon laser scanning fluorescence microscopy. *Science* **248,** 73–76 (1990).
32. Euler, T. *et al.* Eyecup scope–optical recordings of light stimulus-evoked fluorescence signals in the retina. *Pflugers Arch.* **457,** 1393–1414 (2009).
33. Oyster, C. W. & Barlow, H. B. Direction-selective units in rabbit retina: distribution of preferred directions. *Science* **155,** 841–842 (1967).
34. Yamada, E. S. *et al.* Synaptic connections of starburst amacrine cells and localization of acetylcholine receptors in primate retinas. *J. Comp. Neurol.* **461,** 76–90 (2003).
35. Keeley, P. W. *et al.* Dendritic spread and functional coverage of starburst amacrine cells. *J. Comp. Neurol.* **505,** 539–546 (2007).
36. Hausselt, S. E. *et al.* A dendrite-autonomous mechanism for direction selectivity in retinal starburst amacrine cells. *PLoS Biol.* **5,** e185 (2007).
37. Lee, S. & Zhou, Z. J. The synaptic mechanism of direction selectivity in distal processes of starburst amacrine cells. *Neuron* **51,** 787–799 (2006).
38. Oesch, N. W. & Taylor, W. R. Tetrodotoxin-resistant sodium channels contribute to directional responses in starburst amacrine cells. *PLoS ONE* **5,** e12447 (2010).
39. He, S., Jin, Z. F. & Masland, R. H. The nondiscriminating zone of directionally selective retinal ganglion cells: comparison with dendritic structure and implications for mechanism. *J. Neurosci.* **19,** 8049–8056 (1999).
40. Kittila, C. A. & Massey, S. C. Effect of ON pathway blockade on directional selectivity in the rabbit retina. *J. Neurophysiol.* **73,** 703–712 (1995).
41. Caldwell, J. H., Daw, N. W. & Wyatt, H. J. Effects of picrotoxin and strychnine on rabbit retinal ganglion cells: lateral interactions for cells with more complex receptive fields. *J. Physiol. (Lond.)* **276,** 277–298 (1978).
42. Vaney, D. I. & Young, H. M. GABA-like immunoreactivity in cholinergic amacrine cells of the rabbit retina. *Brain Res.* **438,** 369–373 (1988).
43. Fried, S. I., Munch, T. A. & Werblin, F. S. Directional selectivity is formed at multiple levels by laterally offset inhibition in the rabbit retina. *Neuron* **46,** 117–127 (2005).
44. Dmitrieva, N. A. *et al.* Identification of cholinoceptive glycinergic neurons in the mammalian retina. *J. Comp. Neurol.* **456,** 167–175 (2003).
45. Dmitrieva, N. A., Strang, C. E. & Keyser, K. T. Expression of α7 nicotinic acetylcholine receptors by bipolar, amacrine, and ganglion cells of the rabbit retina. *J. Histochem. Cytochem.* **55,** 461–476 (2007).
46. Wickersham, I. R. *et al.* Retrograde neuronal tracing with a deletion-mutant rabies virus. *Nature Methods* **4,** 47–49 (2007).
47. Granstedt, A. E. *et al.* Fluorescence-based monitoring of *in vivo* neural activity using a circuit-tracing pseudorabies virus. *PLoS ONE* **4,** e6923 (2009).
48. Briggman, K. L. & Euler, T. Bulk electroporation and population calcium imaging in the adult mammalian retina. *J. Neurophysiol.* (in the press).

Supplementary Information is linked to the online version of the paper at www.nature.com/nature.

Acknowledgements We thank T. Euler for many useful discussions and help with the functional imaging experiments. We also thank H. Horstmann and S. Mikula for help with staining procedures; J. Kornfeld and F. Svara for programming KNOSSOS; J. Tritthardt for developing electronic circuits and M. Müller for help with the acquisition software; J. Hanne, H. Jakobi and H. Wissler for help with training tracers; M. Feller and Z. J. Zhou for discussion of their results; and J. Bollmann, A. Karpova and S. Seung for comments on the manuscript. We thank N. Abazova, E. Abs, A. Antunes, P. Bastians, M. Beining, J. Buhmann, F. Drawitsch, L. Ehm, F. Isensee, H. Jakobi, S. Kaspar, A. Khan, M. Kiapes, A. Klein, S. Laiouar, E. Möller, J. Trendel, P. Weber, K. Weiß, E. Wiegand and H. Wissler for the tracing work.

Author Contributions K.L.B. and W.D. designed the study; W.D. designed the microtome; K.L.B. performed the calcium imaging and SBEM experiments, K.L.B. and M.H. analysed data; K.L.B., M.H. and W.D. wrote the paper.

Author Information Reprints and permissions information is available at www.nature.com/reprints. The authors declare competing financial interests: details accompany the full-text HTML version of the paper at www.nature.com/nature. Readers are welcome to comment on the online version of this article at www.nature.com/nature. Correspondence and requests for materials should be addressed to K.L.B. (briggman@mpimf-heidelberg.mpg.de).

METHODS

Animals and tissue preparation. Two adult wild-type (C57BL/6) mice were used, one for the calcium-imaging experiment (P29), and one prepared for conventional staining (P30). The mouse used for calcium imaging had been dark-adapted for 2 h before the experiment, with all subsequent procedures up to the functional imaging carried out under dim red illumination. The mice were anaesthetized with Isoflurane (Baxter) inhalation and killed by cervical dislocation. The eyes were enucleated and transferred to a dish containing carboxygenated room-temperature saline, in which the retinas were dissected. All procedures were approved by the local animal care committee and were in accordance with the law of animal experimentation issued by the German Federal Government.

Physiological solutions and calcium-indicator loading. As standard medium we used for tissue dissection, electroporation and recordings a commercially available saline (Biometra) that was supplemented with 0.5 mM L-glutamine and carboxygenated (95% O_2/5% CO_2). To visualize the retinal morphology and the vasculature under the two-photon microscope[32,49] we added sulphorhodamine 101 (SR101, final concentration 0.5–1 μM; Sigma-Aldrich) to the superfusion medium. For the electroporation, a 5 mM solution (in our standard medium) of the synthetic calcium indicator dye Oregon Green 488 BAPTA-1 (OGB-1, hexapotassium salt, Invitrogen) was used. We loaded the ganglion cell layer of the retina by bulk electroporation as described elsewhere (K. L. Briggman and T. Euler, manuscript submitted). Briefly, half of one retina was whole-mounted on filter paper, photoreceptor-side down, and placed between two horizontal parallel-plate electrodes with a 5 μl drop of OGB-1 covering the ganglion cell layer. The electroporation parameters were +13V/2 mm (applied voltage to upper electrode/distance between electrodes), 10-ms pulse width, 1-Hz pulse frequency, 10 square-wave pulses. The retina was immediately transferred to the heated (30–32 °C) recording chamber and allowed to recover for 45 min before two-photon imaging.

Two-photon microscopy. For two-photon imaging[31] we used a custom-built microscope ('eyecup scope'[32]), equipped with through-the-objective light stimulation and two detection channels for fluorescence imaging (red, HQ 622 BP 36, and green, D 535 BP 50 or 520 BP 30; AHF/Chroma). The excitation source was a mode-locked Ti/sapphire laser (Mira-900, Coherent) tuned to ≈930 nm. The microscope was used to simultaneously visualize the retinal structure with SR-101 (red channel, see above) and to monitor calcium activity reflected by OGB-1 fluorescence changes (green channel). During functional imaging, the scan parameters were 64 × 64 pixels at 7.8 Hz frame rate. A marker signal coming from the light stimulator (see next section) was embedded into the image data, at the beginning of each scan line, to allow the registration of calcium signals and stimulus presentations. The imaged field of view for each stimulus presentation was 100 μm × 100 μm. We acquired data from nine such fields, arranged in a 3 × 3 mosaic, for a total recorded area of 300 μm × 300 μm.

Light stimulation. Our light stimulator used custom-written software running under Windows XP to present spatially and temporally structured stimuli on an 800 × 600 pixel miniature LCoS display (i-glasses, EST), alternately illuminated by two band-pass-filtered (blue, 400 BP 20; green, 578 BP 10; AHF/Chroma) LEDs within each frame, for details see ref. 32. We used 'grey' stimuli (with both blue and green LEDs at the same intensity) with a positive contrast, that is, bright foreground on darker background and ~200 and ~60×10^3 photons s^{-1} μm^{-2}, respectively. The LCoS display was coupled into the main optical path of the microscope and, hence, the stimuli were projected onto the retina through the objective lens (XLUMPlanFL 20 × 0.95 NA water-immersion, Olympus). Each of the eight stimuli used was a bar (200 μm wide × 1,000 μm long) moving in one of eight different directions at 0.5 mm s^{-1}.

Calcium-imaging data analysis. Images were analysed offline using custom Matlab (The Mathworks, Inc.) routines. In brief, the pixel intensities within circular regions of interest (ROIs) that were manually placed over each cell body were averaged for each frame. Fractional fluorescence changes were calculated using the mean intensity of each ROI across an entire recording trial as the baseline. The responses to individual stimulus presentations were extracted using the embedded marker signal from the stimulator. The responses were averaged across five stimulus presentations for each of the eight directions. Tuning curves were generated by integrating the total area under the responses and normalizing to the peak integrated area for each cell.

Sample preparation for electron microscopy. We prepared two retinas for electron microscopy; for the first, calcium-imaged retina (e2198) we used a surface-labelling protocol, for the second retina (k0563) we used a conventional staining protocol. Following calcium imaging, e2198 was removed from the recording chamber and placed in 2 ml of room-temperature saline containing 5 mg ml^{-1} horseradish peroxidase (HRP; activity = 1,700 U mg^{-1}, Serva). After 10 min the HRP solution was removed and replaced with fixative solution containing 0.1 M cacodylate buffer, 4% sucrose and 2% glutaraldehyde, pH 7.2 (Serva). The tissue was fixed for 2 h at room temperature and then rinsed in 0.1 M cacodylate buffer + 4% sucrose overnight. A 1 × 1 mm^2 region of the retina centred on the calcium-imaged region was excised and transferred to a solution containing 0.1 M phosphate buffer, 4% sucrose, 5.6 mM diaminobenzidine (DAB: Serva), and 1.4 mM hydrogen peroxide and incubated for 8 h at room temperature. After a 2 h rinse in 0.1 M cacodylate buffer + 4% sucrose, the sample was stained in 2% aqueous osmium tetroxide (Serva) for 2 h at room temperature, and then rinsed in distilled water for 2 h. The osmium-labelled DAB product was further enhanced by en-bloc lead citrate staining, prepared as in ref. 50. The tissue was dehydrated through an ethanol series (70%, 90%, 100%), transferred to propylene oxide, infiltrated with 50%/50% propylene oxide/Epon Hard[51], and then 100% Epon Hard. The block was cured at 60 °C for 24 h.

For conventional staining (k0563), the retina was fixed in 0.1 M cacodylate buffer, 4% sucrose and 2% glutaraldehyde, pH 7.2 for 2 h, then rinsed overnight in 0.1 M cacodylate buffer and 4% sucrose. The tissue was then stained in a solution containing 1% osmium tetroxide, 1.5% potassium ferrocyanide, and 0.15 M cacodylate buffer for 2 h at room temperature[52]. The osmium stain was amplified[53] with 1% thiocarbohydrazide (1 h at 50 °C), and 2% osmium tetroxide (1 h at room temperature). The tissue was then stained with 2% aqueous uranyl acetate for 12 h at room temperature and lead aspartate[54] for 12 h at room temperature. The dehydration and embedding procedures were as described above.

SBEM acquisition. The retinas were cut out of the flat-embedding blocks and re-embedded in Epon Hard, on aluminium stubs for SBEM, with the retinal plane vertical. The samples were then trimmed to a block face of ~200 μm wide and ~400 μm long. Care was taken to trim down the surface of e2198 to just outside the calcium-imaged region, using vasculature landmarks. The samples were imaged in a scanning electron microscope with a field-emission cathode (QuantaFEG 200, FEI Company). Back-scattered electrons were detected using a custom-designed detector based on a special silicon diode (AXUV, International Radiation Detectors) combined with a custom-built current amplifier. The incident electron beam had an energy of 2.5 keV and a current of ~230 pA for e2198 and an energy of 2.0 keV and a current of ~100 pA for k0563. At a pixel dwell time of 1.9 μs and a pixel size of 16.5 nm × 16.5 nm (e2198) and 5 μs and 12 nm × 12 nm (k0563), this corresponds to doses of about 10 (e2198) and 22 (k0563) electrons per nm^2, not accounting for skirting due to low vacuum operation. To prevent charging for e2198, the chamber was kept at a pressure of 50 Pa of water vapour; k0563, which had a higher intrinsic conductivity, was imaged at high vacuum, with the sides of the block evaporation-coated with a 100–200-nm-thick layer of gold. The electron microscope was equipped with a custom-made microtome that is similar to the one described in ref. 25 and is the basis of a commercially available instrument (3view, Gatan). Our microtome allows the repeated removal of the block surface at increments as small as ~23 nm, which was the cutting thickness for e2198 (~25 nm for k0563). 13,000 (for e2198) and 5,760 (for k0563) consecutive block faces were imaged, resulting in data volumes of 3,584 × 21,658 × 13,000 voxels (1 × 7 mosaic of 3,584 × 3,094 images, e2198) and 4,096 × 5,304 × 5,760 voxels (2 × 3 mosaic of 2,048 × 1,768 images, k0563), corresponding to approximate spatial volumes of 60 × 350 × 300 μm^3 and 50 × 65 × 145 μm^3. The edges of neighbouring mosaic images overlapped by ~1 μm. For both retinas, the imaged region spanned the inner plexiform layer of the retina and included the ganglion cell layer and part of the inner nuclear layer. Cross-correlation-derived shift vectors between neighbouring mosaic images and consecutive slices were used for a global least-squares fit across all shift vectors to align the data sets off-line to subpixel precision by Fourier shift-based interpolation. The data sets were then split into cubes (128 × 128 × 128 voxels) for viewing in KNOSSOS.

Skeleton tracing and contact annotation. Skeletons were traced using KNOSSOS (details in M. Helmstaedter, K. L. Briggman and W. Denk, manuscript submitted), and consisted of nodes and connections between them. Nodes could be annotated as needed and were placed approximately every 250 nm. Tracers were instructed to pay attention to branch points and to value accuracy over speed. Typically the cross-sectional view closest to being orthogonal to its axis was used to follow the neurite. The DSGCs were traced by an expert tracer and SACs were traced by trained tracers. Tracers of the very thin SAC dendrites were instructed to skeletonize only those dendrites that could be unequivocally followed. Some branches were, therefore, missed at difficult locations in the data set. As a consequence, some of the SAC skeletons are incomplete (Supplementary Fig. 7). To find potential contact sites, locations were identified where skeletons approached each other more closely than 1.5 μm. Those locations where then manually inspected and classified into putative synapses or incidental contacts. Some of the local contacts were manually volume traced using ITK-SNAP[55].

49. Schlichtenbrede, F. C. *et al.* Toxicity assessment of intravitreal triamcinolone and bevacizumab in a retinal explant mouse model using two-photon microscopy. *Invest. Ophthalmol. Vis. Sci.* **50,** 5880–5887 (2009).
50. Fahmy, A. *An Extemporaneous Lead Citrate Stain for Electron Microscopy* 148–149 (Proc. 25th Annu. EMSA Meeting, 1967).

51. Glauert, A. M. & Lewis, P. R. Biological specimen preparation for transmission electron microscopy. In *Practical Methods in Electron Microscopy* xxi (Princeton Univ. Press, 1998).
52. Karnovsky, M. J. *Use of Ferrocyanide-reduced osmium in electron microscopy* 146 (Proc. 14th Annual Meeting Am. Soc. Cell Biol., 1971).
53. Seligman, A. M., Wasserkrug, H. L. & Hanker, J. S. A new staining method (OTO) for enhancing contrast of lipid-containing membranes and droplets in osmium tetroxide-fixed tissue with osmiophilic thiocarbohydrazide (TCH). *J. Cell Biol.* **30,** 424–432 (1966).
54. Walton, J. Lead asparate, an en bloc contrast stain particularly useful for ultrastructural enzymology. *J. Histochem. Cytochem.* **27,** 1337–1342 (1979).
55. Yushkevich, P. A. *et al.* User-guided 3D active contour segmentation of anatomical structures: significantly improved efficiency and reliability. *Neuroimage* **31,** 1116–1128 (2006).